Building and Environment 293 (2026) 114329

Contents lists available at ScienceDirect

Building and Environment

journal homepage: www.elsevier.com/locate/buildenv

Experimental study on the influence of supply terminal shape on temperature, contaminant distributions and flow characteristics in impinging jet ventilation

Sungeun Lee *, Tomohiro Kobayashi, Haruna Yamasawa, Kentaro Kida

The University of Osaka, 2-1 Yamadaoka, Suita, Osaka, 565-0871, Japan

ARTICLE INFO

Keywords:
Impinging jet ventilation (IJV)
Supply terminal shape
Indoor environment
Ventilation effectiveness
Jet characteristics

ABSTRACT

Impinging jet ventilation (IJV) systems provide higher ventilation effectiveness in the occupied zone compared to traditional mixing ventilation systems. However, IJV system design requires careful consideration of parameters influencing the indoor environment, among which the supply terminal shape could be one of the important parameters. This study aims to investigate the impact of the IJV supply terminal shape on the indoor environment and the impinging jet characteristics. Full-scale experiments were conducted using three different slit-type supply terminals, measuring indoor temperature, CO_2 concentration assuming contaminants, and impinging jet velocity distribution. The experimental results indicated that under the low airflow rate conditions, the supply terminal shape had little impact on the indoor environment, whereas under the high airflow rate conditions, the heat and contaminant removal effectiveness showed a decreasing tendency with increasing the aspect ratio of the supply terminal. The stratification height of CO_2 concentration rose as the airflow rate increased as is well-known, and it was not affected by terminal shape at low supply flow rate conditions. However, when supply airflow rate is large, it was located lower as the aspect ratio of the terminal became higher. Analysis of impinging jet characteristics indicated that a lower aspect ratio of the supply terminal produced more diffusive airflows than the higher aspect ratio terminal. Also, the velocity of the airflow reaching a heating element was higher at the higher aspect ratio conditions. These variations in jet characteristics could affect the indoor environment by changing air distribution patterns and plume flow rate.

1. Introduction

Global warming has promoted worldwide efforts to address climate change, leading many countries to establish specific strategies for net-zero greenhouse gas emissions [1–4]. To achieve this goal, significant changes are needed across many sectors of human activity. Among these, the building sector is especially important due to its substantial contribution to global energy consumption and carbon emissions. Within the building sector, heating, ventilation, and air conditioning (HVAC) systems account for a significant proportion of total energy usage. Hence, it is essential to improve the efficiency of HVAC systems, including air distribution systems. In particular, high-efficiency air distribution systems can create better indoor environments while consuming less energy during the cooling season.

To date, the mixing ventilation (MV) system has been widely used. The MV system mixes the entire room's air with the supplied fresh air, which means the entire room becomes the target of air conditioning. As a result, it has challenges such as relatively high energy consumption and low ventilation efficiency. In contrast, the occupant targeted ventilation system targets local areas such as occupied zones for air conditioning [5]. The displacement ventilation (DV) system, a popular type of OTV system, forms a temperature stratification and contaminant interface layer within a room. As a result, it can create a comfortable environment in the occupied zone and achieve lower energy consumption compared to the MV system in the cooling season [6–8].

Due to the aforementioned benefits of the DV system, several studies have been conducted on the parameters influencing the indoor environment [9,10]. The results confirmed that the indoor environment depends on the momentum of supply air and the buoyancy driven by heat sources. They also showed that a room can be divided into an upper zone and a lower zone by the stratification effect. The upper zone has higher temperature and contaminant concentration, whereas the lower temperature and contaminant concentration are formed in the lower

* Corresponding author.
E-mail address: lee_sungeun@arch.eng.osaka-u.ac.jp (S. Lee).

https://doi.org/10.1016/j.buildenv.2026.114329
Received 6 October 2025; Received in revised form 4 February 2026; Accepted 4 February 2026
Available online 5 February 2026

Nomenclature

Ar_{room}	[-] Dimensionless temperature
A_{inlet}	[-] Area of supply terminal inlet
C	[ppm] CO_2 concentration at any given point
C^*	[-] Dimensionless CO_2 concentration
C_{avg}	[ppm] Averaged CO_2 concentration
C_e	[ppm] Exhaust air CO_2 concentration
C_{max}	[ppm] Maximum value in the vertical profile of average CO_2 concentration
C_{min}	[ppm] Minimum value in the vertical profile of averaged CO_2 concentration
C_r	[ppm] Reference CO_2 concentration for neutral height
C_s	[ppm] Supply air CO_2 concentration
g	[m/s^2] Gravitational acceleration
h	[m] Height for indoor effectiveness calculation
H	[m] Height from floor
h_c	[m] Characteristics length
Q	[m^3/s] Supply airflow rate
T	[-] Temperature at any given point
T^*	[-] Dimensionless temperature
T_{avg}	[°C] Averaged temperature
T_e	[°C] Exhaust air temperature
T_s	[°C] Supply air temperature
U_c	[m/s] Characteristic velocity
r	[m] Radial distance
β	[1/K] Volume expansion coefficient
$\varepsilon_{c,oz}$	[-] Heat removal effectiveness for occupied zone
$\varepsilon_{c,room}$	[-] Heat removal effectiveness for entire room
$\varepsilon_{t,oz}$	[-] Heat removal effectiveness for occupied zone
$\varepsilon_{t,room}$	[-] Heat removal effectiveness for entire room

Subscript

c	Contaminant
e	Exhaust
max	Maximum
min	Minimum
oz	Occupied zone
r	Reference
$room$	Entire room
s	Supply

zone. The height of the interface between them is called stratification height, and designers can control this height by adjusting the supply airflow rate and the plume flow rate from heat sources. In addition, numerous studies have been performed to investigate temperature and contaminant concentration distributions [11–15], and several researchers developed the model to predict the indoor environment, ventilation performance or stratification height [16–23] for practical use.

Even though the DV system provides high ventilation effectiveness and comfortable indoor environments in the occupied zone, it has an overcooling risk at ankle level and limitations when applied to heating or environments with high heat load, as its supply airflow has a low momentum and temperature [6,24].

Another option for high efficiency ventilation is an impinging jet ventilation (IJV) system. To overcome the limitations of the DV system, Karimpanah [25] investigated various types of jets applicable to ventilation systems and identified the potential of impinging jets for the ventilation system. Based on these findings, Karimpanah and Awbi [26] applied IJV to classrooms to investigate its ventilation performance and finally confirmed its applicability.

The IJV system supplies fresh air via supply terminals that are oriented towards the floor, and the air forms the impinging jets when it strikes the floor surface. The impinging jet spreads through the room and is finally exhausted through outlets located on the ceiling after rising by the buoyancy driven by heat sources [27]. Consequently, as with the DV system, the IJV system forms the stratification of temperature and contaminant concentration within a room, thereby enhancing ventilation efficiency. Compared to the DV system, the IJV system produces jets with relatively higher momentum. This characteristic offers distinct advantages in overcoming the limitations caused by the low momentum of the DV jets [28,29]. In the DV system, it is difficult to maintain the temperature difference between head and ankle levels below 3 K, which is recommended to ensure thermal comfort [30,31]. However, the IJV system is expected to mitigate the temperature difference risk through its medium momentum supply, because it promotes the mixing between the jets and the ambient air within the room. It can also be applied to heating operations or situations with high heat loads owing to the same reason [32].

As the IJV system has these advantages, several studies have been conducted on its performance. Ameen et al. [33,34] investigated the thermal comfort and ventilation effectiveness of the IJV system in a cooling mode and found it creates better indoor environments in comparison with the MV system. Also, the IJV system's mean age of air (MAA) is 37 % to 47 % lower than MV, so pollutant and CO_2 concentrations can be effectively exhausted from the occupied zone [35].

Regarding the heating operation, Wang et al. [36] compared the IJV and MV systems based on particle removal performance and confirmed that the IJV system's removal efficiency for fine particles is almost double that of the MV system. Ye et al. [37,38] and Yamasawa et al. [39] reported that the IJV system is applicable in heating operations, and it has better ventilation efficiency and lower energy consumption than the MV system in most operating conditions.

Despite these advantages, the IJV system has not been widely used to date. To promote the adoption of the IJV system for practical use, the performance prediction model for IJV is required. In this regard, zonal models have been proposed to predict temperature and concentration distributions [40,41], and correlations predicting ventilation efficiency were also suggested using the Archimedes number, considering supply airflow rate and heat loads as the parameters [42]. However, the performance of the IJV system is governed by numerous parameters. For instance, Chen et al. [43] have indicated that factors such as the position of external heat loads and the number of occupants significantly influence the airflow patterns and temperature stratification within an IJV-ventilated room. Consequently, further research remains necessary in this area.

Another important factor affecting the indoor environment is the geometrical factor of supply terminals, such as the shape of them. Chen et al. [44] investigated the influence of supply terminal geometry on the flow field under isothermal conditions with a flow rate of 20 L/s (inlet velocity of 1.2 m/s). Four distinct terminal shapes were examined: semi-elliptic, square, and two rectangular forms with aspect ratios (AR) of 2.5 and 10.0. The results indicated that the semi-elliptic terminal facilitated a radial air distribution, exhibiting the most rapid velocity decay in the near-inlet region. In contrast, the rectangular terminal with an AR of 10.0 produced a strong longitudinal discharge along the mainstream direction. This resulted in the slowest velocity decay near the inlet, thereby delaying the establishment of the fully developed flow region. These geometrical effects on the flow field became negligible at a distance of 2.0 m from the supply wall. However, in this study, it remains unclear how these distinct flow characteristics influence on the overall indoor environment.

Staveckis and Borodinecs [45] studied the effects of circular

(DN160), rectangular (0.3 m × 0.075 m), and semi-circular (D_{eq} = 0.25 m) supply terminal shapes on the indoor environment and ventilation efficiency. Under experimental conditions with an airflow rate of 150 m^3/h (1.7–2.1 m/s) and a heat load of 365 W, it was confirmed that the terminal geometry did not significantly influence system performance. Specifically, the variations in contaminant removal effectiveness (1.12–1.16), air exchange effectiveness (0.74–0.83), and heat removal effectiveness (1.14–1.22) were found to be marginal. Regarding relatively high supply airflow rate condition, Wang et al. [46] investigated the impact of terminal shape on heat removal effectiveness with rectangular IJV terminal. Under 750 m^3/h flowrate and 1800 W heat load condition, the results confirmed that when the supply terminal length was extended from 0.2 m to 1.0 m with a fixed width of 0.3 m, the heat removal effectiveness increased by 340 %. Similarly, increasing the width from 0.1 m to 0.5 m with a fixed length of 0.6 m resulted in a 249 % increase in the effectiveness.

In addition to the aforementioned studies, many previous studies [47–49] on supply terminal geometry have demonstrated that the geometry of the supply terminal plays a critical role in indoor environment and airflow characteristics, particularly under high airflow rate conditions. However, many existing literatures have often been conducted without maintaining consistent inlet velocities for comparison, and it remains unclear at which specific airflow rates the terminal shape begins to exert a dominant influence. Therefore, this study investigates the variations in the indoor environment and airflow distribution caused by changes in the supply terminal shape via full-scale experiments. The experiments were conducted under three distinct airflow rate conditions, while using three different slit-type terminals with identical areas but different aspect ratios. Temperature and CO_2 concentration distributions were measured, and the impact of the supply terminal shapes was evaluated in terms of stratification height, contaminant removal effectiveness, and heat removal effectiveness. Furthermore, this study proposes a criterion using the Archimedes number to identify the threshold at which the influence of the supply terminal geometry becomes significant. Based on these results, the formation mechanism of the indoor environment is analyzed, and the findings of this study are expected to serve as a reference for the future design of and research on the IJV system.

2. Full-scale experiment

This section describes the full-scale experiments conducted to investigate the indoor environment and the flow characteristics of impinging jets. First, the experimental setup is introduced. Then, the measuring conditions and methods for indoor temperature and CO_2 concentration distributions are explained. Finally, the process to evaluate velocity distribution within the impinging jets is presented.

2.1. Climate chamber setting

Full-scale experiments were conducted during January and February 2025 in a climate chamber, which has dimensions of 5.45 m (width) × 5.00 m (depth) × 2.77 m (height). The climate chamber is located in a laboratory building at Osaka University, Japan. Fig. 1 (a) and (b) show configuration of the climate chamber and its schematic diagram. As shown in Fig. 1 (b), a total of 11 outlets, which dimensions are 0.58 m × 0.025 m, are installed on the ceiling. In this study, assuming the application of an IJV system into a room with high heat load referring to previous work [50], a heating element with dimensions of 0.80 m × 0.80 m × 0.80 m was placed at the center of the climate chamber. As shown in Fig. 2, the heating element was made of aluminum plates, in which wire-type heaters were installed for heat generation. The heat generation rate was set to 1500 W, which was controlled by a variable autotransformer. To minimize the heat loss from the floor, a rock-wool insulator with a thickness of 0.11 m was placed beneath the heating element, as presented in Fig. 2. Also, to evaluate the indoor environment formed by the 1500 W heating element solely, the experiment was conducted in a controlled environment where no other heat sources were present such as lighting.

2.2. Air supply conditions

Fig. 3 shows the supply terminal dimensions for each shape, and Table 1 shows the experimental conditions.

Referring to Aya et al. [51], the terminal width conditions were set considering 'double-wall' structure concept, which integrates the air supply plenum into the wall cavity to enhance architectural flexibility. From an architectural perspective, minimizing the double wall thickness is desirable to maximize the usable floor area. While the previous study employed a wall thickness (cavity depth) of 0.2 m, three terminal width conditions were set to 0.2 (reference), 0.15, and 0.1 m.

To address the lack of data of previous studies [45,46], the airflow rate conditions were set to 300, 450, and 600 m^3/h, corresponding to the air change rates of 3.97, 5.96, and 7.95 h^{-1} (i.e., the nominal time constants of 0.25, 0.17, 0.13 h). Because, under 1.2 m/s supply velocity condition, the change in the inlet shape causes a clear difference in the indoor airflow distribution [44], dimensions of 0.75 m × 0.2 m were selected as a reference case (Case 1), yielding a supply velocity of 1.11 m/s (similar to the previous study condition 1.2 m/s) at 600 m^3/h condition.

To set the same supply velocity condition with the same flowrate, the supply area conditions were maintained constant at 0.15 m^2 across all

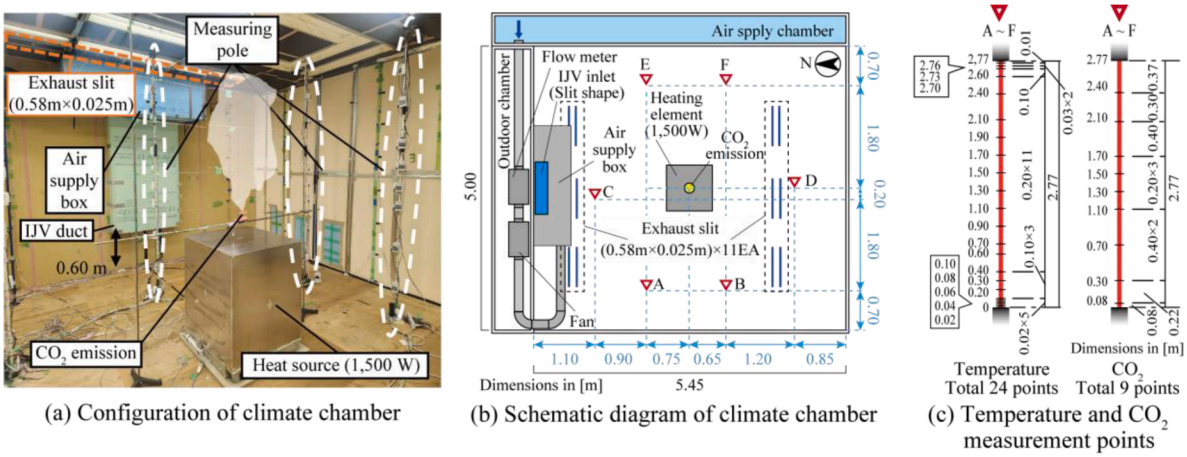

(a) Configuration of climate chamber (b) Schematic diagram of climate chamber (c) Temperature and CO_2 measurement points

Fig. 1. Climate chamber and measurement points for indoor environment.

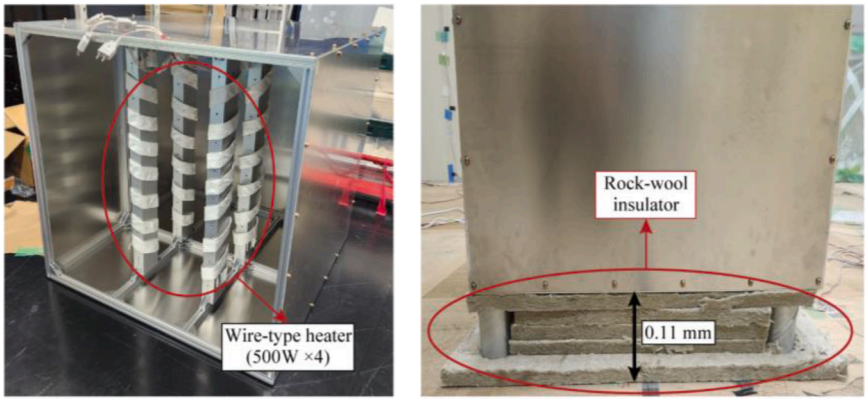

Fig. 2. Heating element.

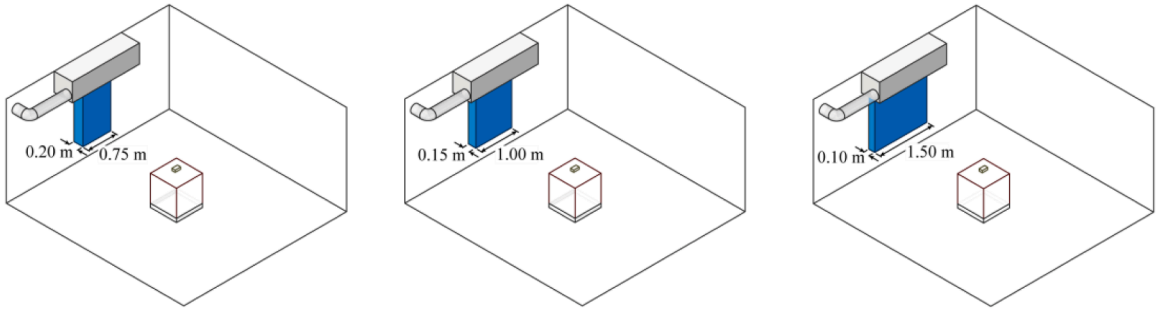

Fig. 3. Dimensions of supply terminal.

Table 1
Indoor environment measurement conditions.

Case ID	Heat load [W]	Duct size [$m \times m$]	Aspect ratio [-]	Airflow rate [m^3/h]	Nominal supply velocity [m/s]	Air change rate [1/h]	Nominal time constant [h]	Supply temperature [°C]	CO_2 emission rate [Nm^3/h]
Case 1 - 300	1500	0.75 × 0.20	3.75	300	0.56	3.97	0.25	2.68	0.30
Case 1 - 450				450	0.83	5.96	0.17	3.60	0.45
Case 1 - 600				600	1.11	7.95	0.13	6.04	0.54
Case 2 - 300		1.00 × 0.15	6.67	300	0.56	3.97	0.25	2.55	0.30
Case 2 - 450				450	0.83	5.96	0.17	3.50	0.45
Case 2 - 600				600	1.11	7.95	0.13	5.80	0.54
Case 3 – 300		1.50 × 0.10	15	300	0.56	3.97	0.25	2.77	0.30
Case 3 – 450				450	0.83	5.96	0.17	3.89	0.45
Case 3 - 600				600	1.11	7.95	0.13	6.16	0.54

cases, Consequently, the three different inlet shape conditions were set to 0.75 m × 0.20 m, 1.00 m × 0.15 m, and 1.50 m × 0.10 m.

Regarding the air supplying method, an air supply box was fabricated from extruded polystyrene foam, referring to the air supply structure used in a study related to wall-attachment ventilation [52]. Fig. 4 shows schematic diagrams of the air supply box for each slit size. Inside the air supply box, a perforated plate was installed to achieve a uniform air velocity distribution at the discharge plane. From the air supply chamber adjacent to the climate chamber, low-temperature air was supplied into the room through the air supply box and the slit-type terminal. This terminal was installed at the center of the north wall at a height of 0.60 m from the floor. Both the duct and air supply box were insulated to reduce heat loss. The air supplied into the room was exhausted through ceiling-mounted exhaust slits.

The supply airflow rate was adjusted using fans positioned on both the supply and exhaust sides. It was measured with a flow meter (New Aero AE150D, ±3 % R.D., Wetmaster Co. Ltd.) installed in an insulated outdoor air chamber located adjacent to the climate chamber. To minimize the overall heat transfer through other walls of the climate chamber, the supply air temperature was set to low temperature values for each condition. By adjusting the setting temperature of air-handling unit for the air supply chamber, the supply temperature was controlled

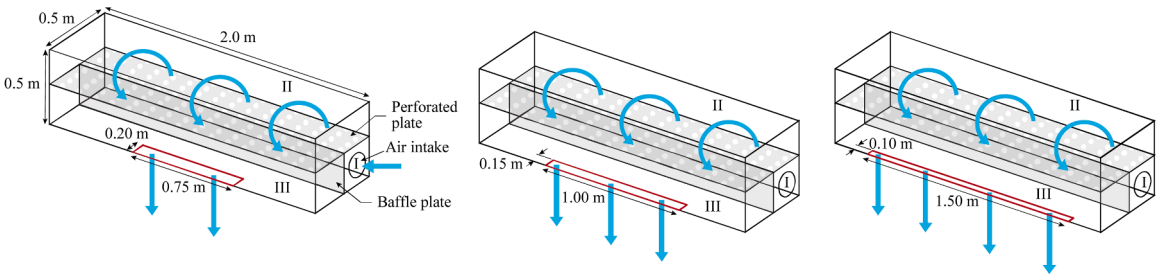

(a) 0.75 m × 0.20 m (b) 1.00 m × 0.15 m (c) 1.50 m × 0.10 m

Fig. 4. Structure of air supply box.

to ensure the heat transfer rate, calculated from the temperature difference between supply and exhaust air, was approximately 1500 W. Here, it must be noted that this treatment was necessary to minimize the effect outdoor temperature for each case because the experiment was carried out in midwinter. This temperature shift does not lead to any loss in generality in the experimental results. Also, the difference in supply temperatures is because changing the supply airflow rate causes the difference in indoor temperature distribution, and the outside temperature for each case was different depending on the day.

2.3. Measurement of temperature and CO_2 concentration

For the purpose of evaluating contaminant concentration distributions, CO_2 was released at a height of 0.14 m above the heating element (1.05 m from the floor). The CO_2 was supplied through a tube, which is connected with the CO_2 cylinder. To minimize any potential influence on the indoor airflow, the tube outlet was covered with a porous medium (sponge, 0.105 m × 0.075 m × 0.035 m), as shown in Fig. 1 (a). Also, based on the expectation that the high heat load would generate a thermal plume strong enough to effectively entrain the released CO_2 into the thermal plume flow, the CO_2 was released solely. The emission rates were adjusted to 0.30, 0.45, and 0.54 Nm^3/h for the 300, 450, and 600 m^3/h airflow conditions, respectively. These rates, controlled by a mass flow controller, were chosen to target a CO_2 concentration difference of approximately 1000 ppm between the inlet and outlet accounting for experimental accuracy and CO_2 datalogger's uncertainty. At the measuring poles A to F shown in Fig. 1 (b), temperature and CO_2 concentration distributions were measured at 24 and 9 points, respectively, in the vertical direction, as illustrated in Fig. 1 (c). Type-T thermocouples (ASTM E230 Standard class, ±1 °C or ±0.75 %) and CO_2 data loggers (RTR-576, T&D Co., Ltd.) were used for temperature and CO_2 concentration measurements, respectively.

All CO_2 data loggers were calibrated in a two-step process.

In the Primary calibration (Standard span gas → Reference loggers) step, three reference loggers were calibrated using standard span gases at four known concentrations (i.e. C_{true}: 400, 1000, 1500, 2000 ppm). Least square method was applied to establish the relationship between the true values (C_{true}) and the measured values ($X_{measured}$) and the true concentrations, expressed as $C_{true} = a \times X_{measured} + b$. By this equation, we can calculate the true value from logger readings. The calibration achieved high accuracy with respect to the true values, yielding an average and maximum RMSE of 3.9 ppm and 7.7 ppm, respectively.

Next, in the Cross-Calibration (Reference loggers → The other loggers) step, the remaining loggers were cross-calibrated against the verified reference units within a mixing chamber using a concentration decay method. Data were collected across a range of 460–3500 ppm (540 points per logger) as the concentration gradually decreased to outdoor CO_2 levels. By treating the reference logger readings as true values, calibration equations were derived, resulting in an average and maximum RMSE of 8.4 ppm and 14.0 ppm, respectively.

All measurements were conducted at 1-minute intervals. After the temperature and CO_2 concentrations reached a steady state, data was acquired for a 30-minute period. The average values from this period were used as the final experimental results. Also, during the experiments, all measurements were conducted under fully automatic and unattended conditions to eliminate disturbances caused by human metabolic heat and movement.

2.4. Measurement of velocity distribution

Table 2 illustrates the measurement conditions of velocity distribution. The airflow rate was fixed at 600 m^3/h, since the influence of airflow momentum is dominant relative to buoyancy in this condition. This dominance makes the most evident impact of airflow changes induced by the supply terminal shape on the temperature and CO_2 distribution, as will be shown in Section 3.2. To investigate the velocity distribution at the supply terminal and the characteristics of impinging jets, the measurements were carried out at the inlet plane, center plane, side plane, and diagonal plane, as shown in Fig. 5. In Case 3, where the velocity distribution at the supply terminal inlet was relatively uniform, measurements were conducted on the right-side and right-diagonal plane (Fig. 5). In contrast, for Case 1 and Case 2, where asymmetry was observed in the supply velocity distribution, additional measurements were also performed on the corresponding left-side planes. This will be discussed in Section 3.3.1.

Table 2
Velocity measurement conditions.

Case ID	Airflow rate [m^3/h]	Duct size [m × m]	Measurement plane	Measurement devices	The number of measurement points
Case 1	600	0.75 × 0.20	Inlet	I-type hot-wire anemometer	21
			Center	Ultrasonic velocimetry, multi-point omnidirectional anemometer	102
			Right side		102
			Right diagonal		102
			Left side		102
			Left diagonal		102
Case 2		1.00 × 0.15	Inlet	I-type hot-wire anemometer	21
			Center	Ultrasonic velocimetry, multi-point omnidirectional anemometer	102
			Right side		102
			Right diagonal		102
			Left side		102
			Left diagonal		102
Case 3		1.50 × 0.10	Inlet	I-type hot-wire anemometer	20
			Center	Ultrasonic velocimetry, multi-point omnidirectional anemometer	102
			Right side		102
			Right diagonal		102

Inlet plane: isothermal / Center, side, diagonal plane: non-isothermal.

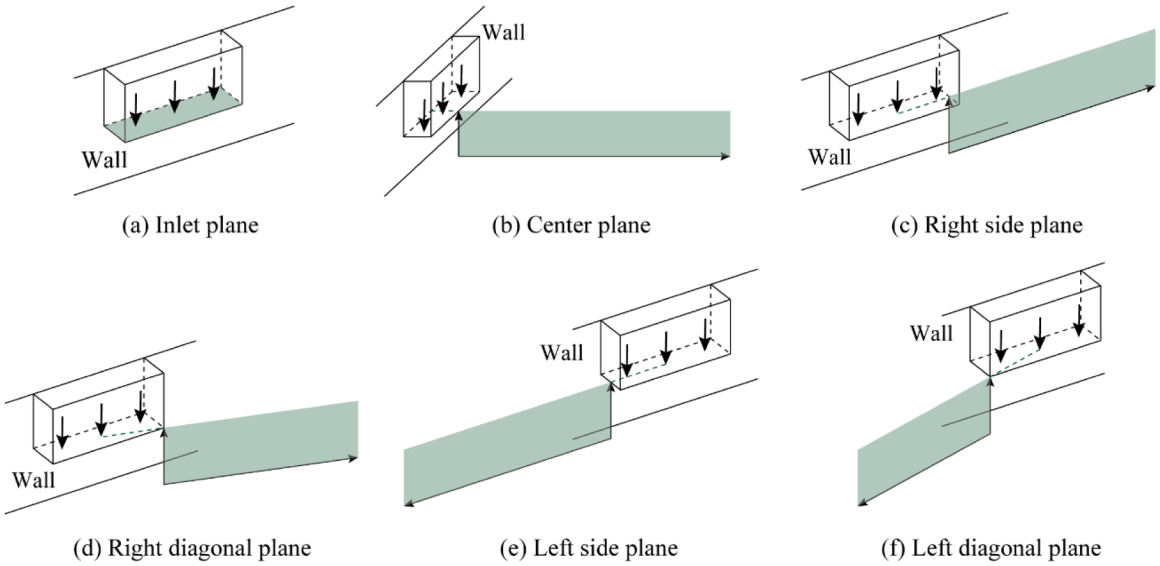

Fig. 5. Measurement plane for velocity distribution.

Using a hot-wire anemometer (Fig. 7 (a)), The number of measurement points at the inlet plane was set to 20 or 21 depending on the supply terminal dimension so that the overall velocity distribution was captured, as presented in Fig. 6 (a)-(c). In each measurement plane for impinging jets, velocity distribution was measured up to a height of 0.24 m from the floor and up to 1.00 m from the end of the supply terminal, as depicted in Fig. 6 (d). As shown in Fig. 7 (b)-(c), three-dimensional velocity was measured with an ultrasonic anemometer (TR-92T, ±3 % R.D. ±0.05 m/s, SONIC Co. Ltd.), while velocity magnitude was measured with multi-point omnidirectional anemometers (Multi-Channel Anemomaster PRO 0975–21, ±2 % R.D. or 0.02 m/s, KANOMAX Co. Ltd.). For each point, the average value of the velocity data collected over one minute was used as the final results. In those planes, the intervals between each measurement point were determined as follows; 0.20 m in the mainstream (horizontal) direction, 0.01 m intervals from the floor to 0.10 m, and 0.02 m intervals from 0.10 m to 0.24 m in the vertical direction. For the ultrasonic anemometer, measurements were performed from a height of 0.03 m above the floor to avoid contact between the probe and the floor.

2.5. Verification of experimental reliability

Given the prohibitive time costs associated with full-scale experimentation, full replicates for all conditions were not feasible. Instead, to

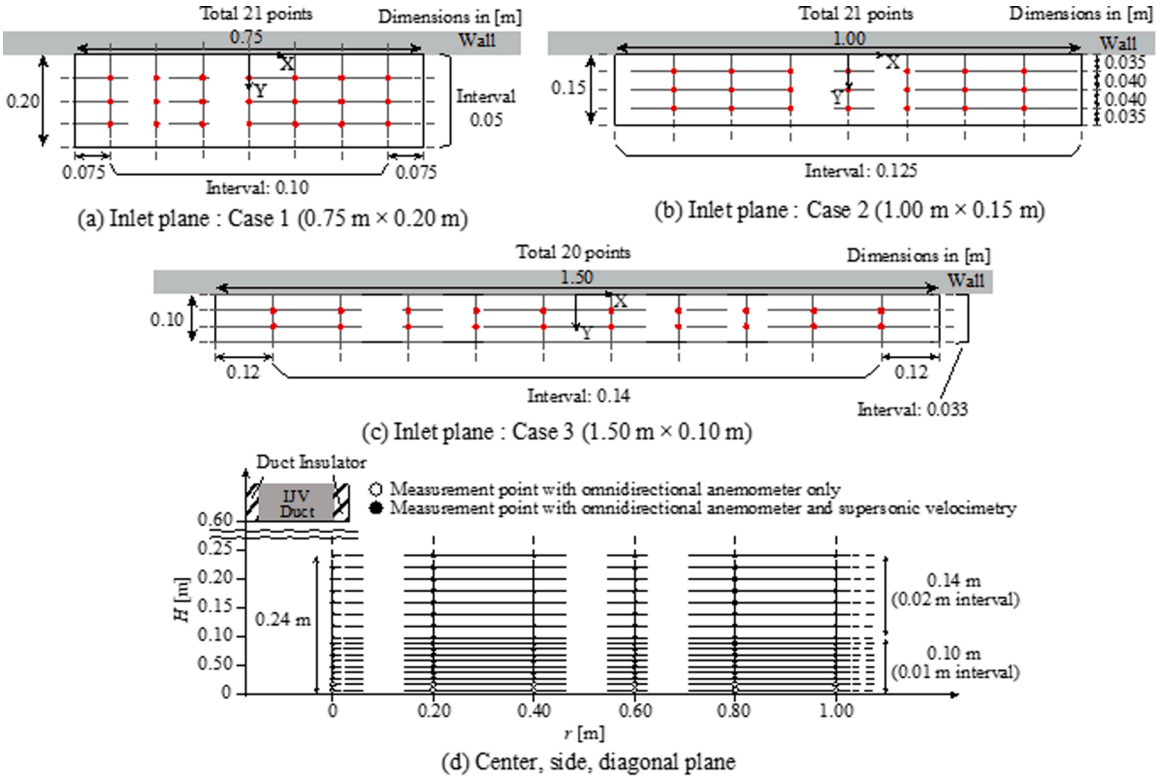

Fig. 6. Points for velocity measurement.

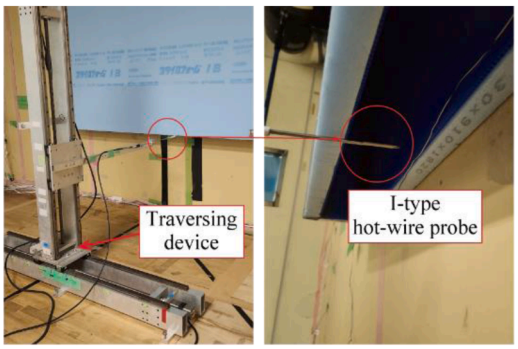

(a) Hot-wire anemometer

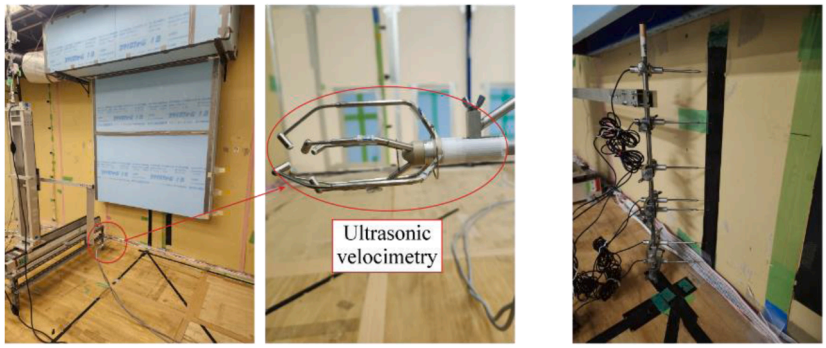

(b) Ultra-sonic velocimetry (c) Omnidirectional anemometer

Fig. 7. Velocity measurement device.

ensure data reliability, three independent replicate experiments were conducted for a representative reference case (IJV circular 300Φ, 600 m^3/h) before the experiments with the slit-type supply terminals. Since all cases utilized identical instrumentation setup, the repeatability demonstrated in this reference case is considered applicable to the entire dataset.

The error analysis confirmed high repeatability across all measured variables. For temperature distribution, analyzed based on the temperature difference ($T\text{-}T_{supply}$), the average coefficient of variation (CV) was 1.72 %. CO_2 concentration measurements yielded an average CV of 2.18 %. Regarding velocity distribution, ultrasonic velocimetry measurements showed an average CV of 3.75 %, with relatively great deviations primarily confined to low-velocity regions. Additionally, data from the omnidirectional anemometer were validated through cross-comparison with the ultrasonic velocimetry results, exhibiting overall consistent velocity profiles. Detailed results of the error analysis are provided in the Supplementary Material.

3. Result and discussion

3.1. Definition of indices

This section defines the indices used in this paper. Since the aim of this study is to investigate the influence of the supply terminal shapes on the indoor environment, the following indices are used: i) Dimensionless temperature, ii) Heat removal effectiveness (HRE), iii) Dimensionless CO_2 concentration, iv) Contaminant removal effectiveness (CRE), and v) Stratification height. Finally, Archimedes number, a dimensionless number determined by the experimental condition (airflow rate and heat load), is also defined. i) Dimensionless temperature

The overall heat transfer rate through the walls varied slightly between cases due to differences in the outdoor air temperature. This variation led to a slight change in the temperature difference between the supply and exhaust air, although this effect was minimized by adjusting the supply temperature as previously mentioned. Therefore, to eliminate this influence and express temperature profile in a general form, a dimensionless temperature (T^* [-]), which is defined as Eq. (1), is used for the analysis of the temperature distribution.

$$T^* = (T - T_s)/(T_e - T_s) \tag{1}$$

where T [°C] is the temperature at any given measurement point, while T_e [°C] and T_s [°C] denote the exhaust and supply temperature, respectively. ii) Heat removal effectiveness

Heat removal effectiveness (ε_t [-]) is an index that evaluates how effectively a ventilation system removes heat in a room [53]. By definition, the average HRE and the average dimensionless temperature have an inverse relationship. It is defined as:

$$\varepsilon_t = \frac{T_e - T_s}{T_{avg} - T_s} = \frac{T_e - T_s}{\frac{1}{h}\int_0^h T dh - T_s} \tag{2}$$

where T_{avg} [°C] is the spatially averaged temperature of targeted space, and h [m] is height of target space.

In this study, the indoor environments of the entire room and the occupied zone were evaluated by this index. Generally, the ε_t [-] value is calculated based on the volume-averaged temperature. However, in this study, the value (e.g., mean temperature) was calculated using a height-based integration of the measurement poles, assuming that each pole represents an equal horizontal area. Furthermore, the purpose of this index is to quantitatively compare the indoor environmental changes caused by different supply terminal shapes. Since the region of interest for this comparison is the ambient zone outside the thermal plume, temperatures within the plume region were excluded from the calculation.

For the $\varepsilon_{t,room}$ [-] calculation, which targets the entire room, h [m] was set to the ceiling height of 2.77 m, and 144 measured data were used (24 points / pole × 6 poles). For the calculation of $\varepsilon_{t,oz}$ [-], the occupied zone was defined as the space from 0 m to 1.8 m, based on SHASE

Standard 102 in Japan [54]. However, the h [m] used in the $\varepsilon_{t,oz}$ [-] calculation was set to 1.7 m, which corresponds to the height of the highest measurement point within this defined zone. The number of measured points used for $\varepsilon_{t,oz}$ calculation was 96 (16 points / pole × 6 poles). iii) Dimensionless CO_2 concentration

Since the inlet and outlet CO_2 concentrations varied between cases, a dimensionless CO_2 concentration C^* [-] is used to evaluate the CO_2 concentration distributions under consistent criteria. C^* [-] is given by Eq. (3):

$$C^* = (C - C_s)/(C_e - C_s) \tag{3}$$

where C [ppm], C_e [ppm], and C_s [ppm] denote the CO_2 concentration at some measurement point, the exhaust, and the supply, respectively. iv) Contaminant removal effectiveness

Contaminant removal effectiveness (ε_c [-]) is an index that evaluates how effectively a ventilation system removes contaminants from a room [55]. It compares the concentration in the exhaust with the mean concentration in any given space, and the definition is shown in Eq. (4).

$$\varepsilon_c = \frac{C_e - C_s}{C_{avg} - C_s} = \frac{C_e - C_s}{\frac{1}{h}\int_0^h C dh - C_s} \tag{4}$$

where C_{avg} [ppm] is the spatially averaged temperature of targeted space.

For the CRE calculation of the entire room and occupied zone, the same criteria for 'h' and calculation method used for HRE calculation were applied. As a result, the CRE of entire room was based on 54 (9 points / pole × 6 poles), and that of occupied zone is calculated with 42 points (7 points / pole × 6 poles). v) Stratification height (CO_2 concentration interface)

Stratification height is an important parameter that represents the characteristics of a stratified ventilation system. Li [56] introduced that, assuming one-dimensional flow and steady state, the simplified temperature interface height can be defined as the height at which the temperature equals the average of the inlet and outlet temperatures (i.e., the reference temperature). Based on this concept, this study defines a simplified stratification height to evaluate the stratification characteristics for each condition. The height is defined based on the CO_2 concentration results, as they showed a more distinct interface compared to the temperature distribution results. However, since the results showed that the minimum dimensionless CO_2 concentration for each case was non-zero, the reference concentration for the simplified stratification height is defined by Eq. (5).

$$C_i = (C_{min} + C_{max})/2 \tag{5}$$

Here, C_{min} [ppm] and C_{max} [ppm] are calculated from the vertical profile of horizontally averaged CO_2 concentration. Here, the vertical profile represents the distribution in the vertical (height) direction of the average CO_2 concentration values measured at poles A-F at each height. The minimum value in this profile is defined as C_{min}, and the maximum value is defined as C_{max}. In this paper, the simplified stratification height indicates the height at which the value of C_i [ppm] is obtained.

While alternative methods [21,22] for defining the stratification height exist, the current method was adopted because it most effectively explains the experimental results.

Finally, the Archimedes number (Ar) is used as the index to represent the overall characteristics of indoor environment. According to Nielsen [57], flow patterns in a room can be classified based on this index. For this reason, it is used in several studies to develop empirical correlations for indoor environmental evaluation [33,39,58,59]. The Archimedes number for a room (Ar_{room}) is defined as follows:

$$Ar_{room} = g\beta h_c (T_e - T_s)/U_c^2 \tag{6}$$

where g [m/s^2] is gravitational acceleration and β is the thermal expansion coefficient of air. h_c [m] and U_c [m/s] represent the characteristic length and velocity, respectively; The height of room and supply velocity (Q [m^3/s] / A_{inlet} [m^2]) were adopted for these parameters.

3.2. Temperature and CO_2 concentration

Table 3 presents the Ar_{room}, HRE, and CRE for each case. The Ar_{room} values reveal that cases with identical supply airflow rate conditions have almost identical Ar_{room} values. This is because both supply velocity and temperature difference between supply and exhaust air are almost same among three cases at the same supply flow rate. Therefore, by comparing the three cases under the same Archimedes number (Ar_{room}), the influence of the supply terminal shape alone on the indoor environment can be discussed. As for the results of HRE and CRE, they are discussed in Section 3.2.3. Finally,

3.2.1. Dimensionless temperature distribution

Fig. 8 (c-1) to (c-3) show the vertical profiles of dimensionless temperature measured at poles A to F, and Fig. 8 (b-1) to (b-3) present the vertical profiles of horizontally averaged values for all poles.

The results confirmed that thermal stratification was formed at the location of each pole under all conditions. The average dimensionless temperature distribution revealed that the influence of supply terminal shape was different depending on the supply airflow rate condition. Under the supply airflow rate of 300 m^3/h, no significant difference was caused by variation in supply terminal shape. However, as the supply airflow rate increased, the influence of supply terminal shape became more evident. Specifically, in the cases of 600 m^3/h, the temperature measured at any given height was lowest in the case of the smallest aspect ratio (Case 1), whereas larger aspect ratios resulted in higher temperatures.

This difference in tendency with supply flow rate seems to be caused by the ratio of momentum to buoyancy. Under the 300 m^3/h condition, the Ar_{room} is the highest, indicating a relatively low momentum force compared to buoyancy. In other words, a buoyancy-dominated flow field is formed. Although the supply terminal shape could affect the momentum of the jet spreading into the indoor space, its influence is

Table 3
Experimental result - indoor environment.

Case ID	Aspect rati [-]	Airflow rate [m^3/h]	Ar_{room} [-]	$\varepsilon_{t,\ room}$ [-]	$\varepsilon_{t,\ oz}$ [-]	$\varepsilon_{c,\ room}$ [-]	$\varepsilon_{c,\ oz}$ [-]
Case 1 - 300	3.75	300	3.65	1.38	1.63	1.56	2.08
Case 1 – 450		450	1.19	1.46	1.81	1.95	3.12
Case 1 – 600		600	0.51	1.54	2.00	2.38	4.54
Case 2 - 300	6.67	300	3.68	1.37	1.62	1.63	2.18
Case 2 – 450		450	1.23	1.44	1.76	1.96	3.05
Case 2 – 600		600	0.53	1.49	1.89	2.18	3.77
Case 3 - 300	15	300	3.58	1.36	1.58	1.62	2.18
Case 3 – 450		450	1.22	1.38	1.64	1.91	2.85
Case 3 – 600		600	0.51	1.40	1.69	1.96	3.03

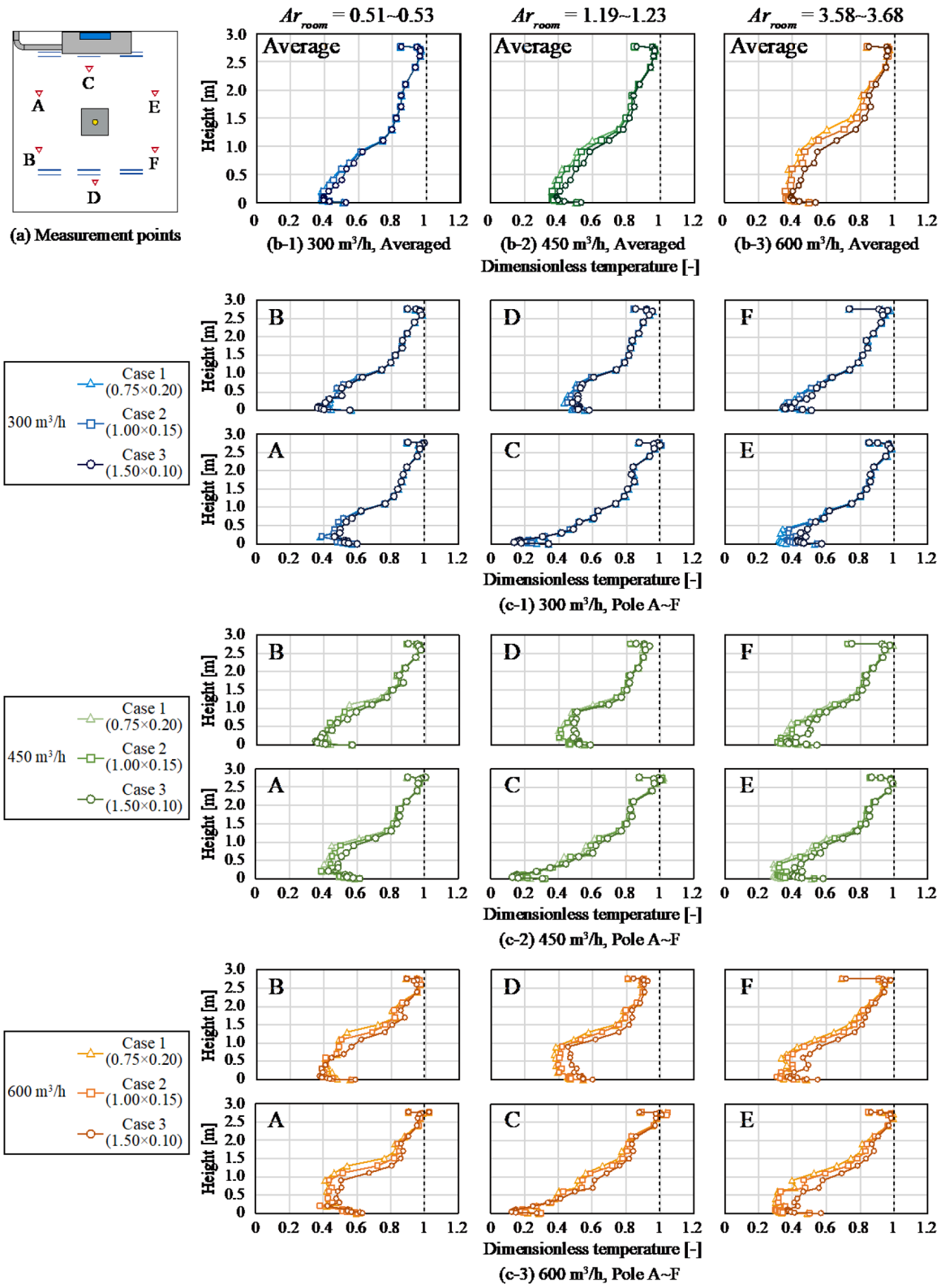

Fig. 8. Vertical profile of dimensionless temperature.

expected to be limited in such a buoyancy-dominated flow field. In contrast, under the conditions of 600 m^3/h, the influence of momentum force becomes more significant in comparison with buoyancy, leading to pronounced differences in temperature distribution depending on the supply terminal shape. Consequently, it could be concluded that the supply terminal shape has little impact on temperature profile when Ar_{room} is large, while it cannot be ignored when Ar_{room} is small.

3.2.2. *Dimensionless CO2 concentration*

Fig. 9 (c-1) to (c-3) present the vertical profiles of dimensionless CO_2 concentration, and Fig. 9 (b-1) to (b-3) show the vertical profiles of horizontal averages for all poles and the simplified stratification heights.

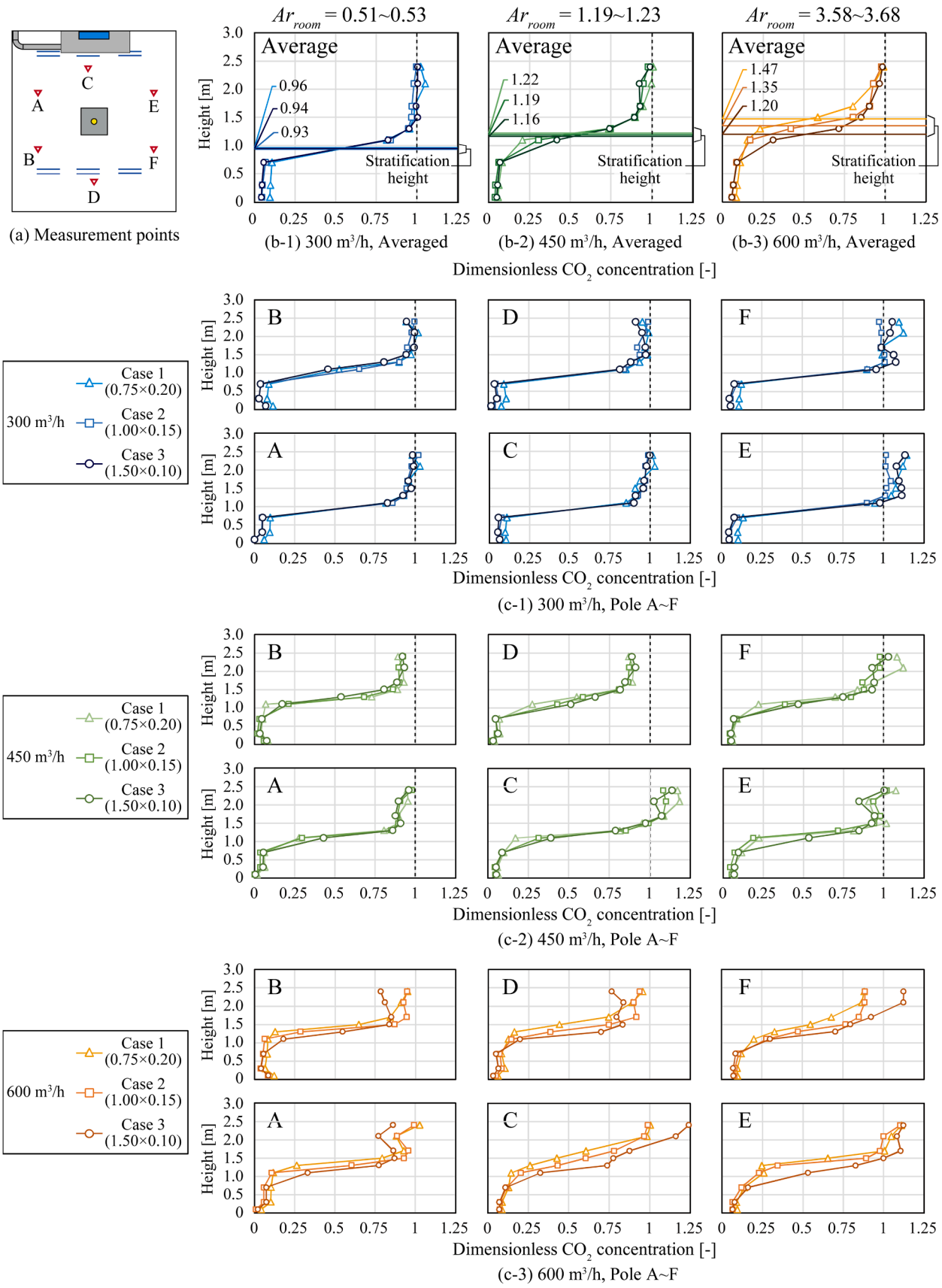

Fig. 9. Vertical profile of dimensionless CO_2 concentration.

In this study, experiments were conducted under high heat load conditions, resulting in a strong thermal plume. This plume transported CO_2 emitted from the top of the heating element to the upper zone of the room, creating a distinct CO_2 concentration difference between the upper and lower zones in the room.

Similar to the results of temperature distribution, no significant differences were observed among the cases with the supply airflow rate of 300 m^3/h. However, at higher supply airflow rates, the terminal shape had a distinct influence on the CO_2 concentration distribution. At a supply airflow rate of 600 m^3/h conditions, the effect of supply terminal shape on CO_2 concentration distribution was similar to that of the temperature distribution: a smallest aspect ratio (Case 1) generally exhibited the lowest CO_2 concentrations, while larger aspect ratio conditions resulted in higher concentration. Nevertheless, below the CO_2 emission height (1.05 m), the differences in CO_2 concentration among the cases were negligible.

Regarding the fluctuations of CO_2 concentration in Fig. 9(c-3), advection driven by indoor recirculation flow becomes dominant under high airflow conditions. This likely creates non-uniform contaminant distributions in the upper zone, resulting in local concentration variations even under identical terminal shape conditions.

Under the identical terminal shape conditions, the simplified stratification height became higher as the supply airflow rate increased. Since the stratification height is known to form at the height where the supply airflow and thermal plume flow rates are equal, this result is consistent with previous studies [9,10,56,60].

Additionally, under the 300 m^3/h conditions, the stratification height did not differ significantly depending on the supply terminal shape. However, at the 600 m^3/h conditions, the stratification height in the case of the smallest aspect ratio (Case 1) was approximately 0.27 m higher than that of the largest aspect ratio (Case 3). These results can also be attributed to the difference in the ratio of momentum to buoyancy between Case 1 and Case 3, as described in Section 3.2.1. This tendency implies that the supply terminal shape influences the thermal plume flow rate under high airflow conditions. Verifying this interaction requires further detailed experimental or numerical investigations focusing on the thermal plume.

Consequently, consistent with the conclusion of Section 3.2.1, the CO_2 concentration distribution and stratification height are unaffected by the supply terminal shape in the high Ar_{room} (buoyancy-dominated) regime. However, they exhibit significant variations depending on the terminal shape in the low Ar_{room} (momentum-dominated) regime.

3.2.3. Heat/Contaminant removal effectiveness

In this section, the results of HRE and CRE for both the entire room and the occupied zone are presented. The data for HRE and CRE are shown in Table 3 and Fig. 10.

For a given supply terminal shape, both HRE and CRE increased with the supply airflow rate, and the rate of increase in CRE was higher than that of HRE. This is because stratification height tends to be higher as the supply airflow rate increases, which in turn leads to a decrease in the average temperature and CO_2 concentration, especially in the occupied zone.

At high supply airflow rates, the influence of the supply terminal shape on HRE and CRE was distinct, which is consistent with the results for the temperature and CO_2 concentration distributions. At the airflow rate of 600 m^3/h, both HRE and CRE decreased with an increase in the aspect ratio of the supply terminal. This variation was more pronounced in the results of CRE. This tendency is considered to result from the fact that these indices are the functions of average temperature and average CO_2 concentration. This means that they vary significantly when the temperature distribution or CO_2 concentration distribution shows a large difference. As confirmed in Sections 3.2.1 and 3.2.2, the dimensionless temperature values are higher than dimensionless CO_2 concentration values in the region below the stratification height, because source locations and the transport mechanisms between heat and CO_2 are different. Specifically, the CO_2 was released solely from the top of the heat source, resulting in negligible concentration changes in the lower portion of the room. In contrast, heat transfer occurs not only from the top surface but also through convective heat exchange along the side

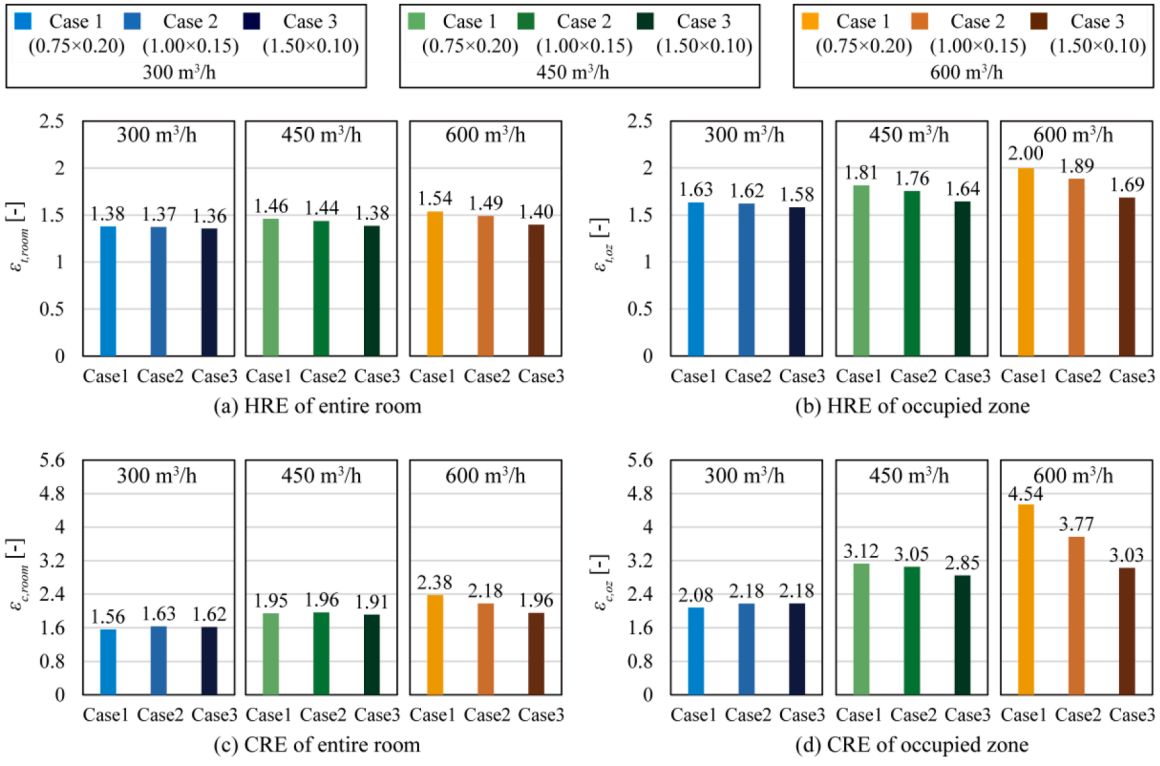

Fig. 10. Heat / Contaminant removal effectiveness.

surfaces of the heat source. This convective mechanism leads to higher dimensionless temperature values in the lower zone compared to the dimensionless CO_2 concentration. Furthermore, radiative heat transfer also contributes to the diffusion of heat, causing the vertical temperature profile to deviate from the concentration profile [22].

Consequently, these distributional differences make the average dimensionless CO2 concentration more sensitive to terminal shape variations than temperature. This greater sensitivity accounts for the larger rate of change observed in CRE compared to HRE. Also, both indices were higher in the occupied zone than in the entire room. This reflects the primary influence of the supply terminal shape on the occupied zone, consistent with the stratification height analysis.

3.2.4. Ar_{room} threshold for terminal shape dependency

The results in Sections 3.2.1–3.2.3 confirmed that the dependence of indoor temperature and CO_2 concentration on the supply terminal shape varies according to the Ar_{room} value, which subsequently impacts HRE and CRE. Based on these findings, this section proposes an Ar_{room} threshold regarding this dependency and discusses its limitations and applicability.

The results in Fig. 8 (b) and Fig. 9 (b) demonstrate that the temperature and CO_2 concentration distributions vary depending on the supply terminal shape when the airflow rate is larger than 450 m^3/h (Ar_{room} =1.19~1.23). Also, as shown in Fig. 10, it is observed that the HRE and CRE values in occupied zone also vary depending on the supply terminal shape within the same airflow rate range (larger than 450 m^3/h). Therefore, the Ar_{room} threshold at which the indoor environment starts to vary depending on the supply terminal shape was determined to be approximately 1.2.

In this study, experiments were conducted using slit-type terminals. Since the threshold was derived based on these specific results, further investigation is required to verify its applicability to other terminal shapes (e.g., circular or semi-elliptical) and heat source conditions. However, specifically for designs utilizing slit-type terminals, the proposed Ar_{room} threshold serves as a quantitative verification criterion for determining supply terminal geometries during the initial design phase.

If the calculated Ar_{room} value is within the buoyancy-dominated regime ($Ar_{room} > 1.2$), the influence of the terminal shape on the indoor environment is negligible. In this scenario, the terminal shape can be selected based primarily on economic factors, such as cost and constructability. Conversely, in the momentum-dominated regime ($Ar_{room} < 1.2$), the indoor environment becomes sensitive to the supply airflow characteristics. Under these conditions, employing low-aspect-ratio terminals is recommended. Also, as will be discussed in Section 3.3.2, these shapes generate a highly diffusive airflow with relatively low velocity, resembling a radial jet. Consequently, improvements in thermal comfort, such as a reduced risk of draught, are also expected.

3.3. Velocity distribution

In Section 3.2, the experimental results of temperature and CO_2 concentration distribution were shown and discussed. Although significant differences were observed depending on the supply terminal shapes under the high supply airflow rate conditions, further investigation is required to understand the underlying causes. With respect to this, it is conjectured that the differences in supply terminal shape produce variations in indoor airflow, thereby causing changes to the indoor environment.

This section presents the measurement results of velocity distributions at the supply terminal inlet and impinging jet and analyzes the characteristics of the velocity distribution. In addition, the influence of the velocity distribution on the indoor environment is discussed.

3.3.1. Velocity distribution over the supply terminal inlet

The velocity distributions at the supply terminal inlet measured by a hot-wire anemometer are shown in Fig. 11. When viewing from the front side of the terminal, Case 1 and Case 2 showed a higher velocity at the left side (negative coordinate in X direction) than the opposite side. On the contrary, almost uniform velocity distribution was formed in Case 3. This seems to be driven by the structure of the air supply box. As shown in Fig. 4, region III in the air supply box is an empty space. In Case 3, the length of the discharge area has a large portion of the air supply box, which results in a smooth air supply and the uniform velocity distribution. However, in Case 1 and Case 2, the length of the discharge area is relatively short compared to that of the air supply box. As a result, airflow stagnation and eddy formation could occur on the side opposite the air intake, resulting in these low-velocity distribution.

Because these non-uniform velocity distributions could create a different indoor environment from that with uniform velocity distribution, the velocity contours at the right and left sides were compared based on the measurement results of the omnidirectional anemometer, as shown in Fig. 12. The velocity contours in the side planes for both Case 1 and Case 2 showed asymmetric velocity distribution, while relatively symmetrical contours were observed at the diagonal plane. Although asymmetric velocity distributions were observed at the side plane, the extent to which this non-uniformity influences the overall indoor thermal environment and airflow patterns has not been fully quantified in this study. Therefore, a comparison with a uniform supply condition, via additional experiments or CFD simulations, remains a subject for future work.

3.3.2. Vertical velocity distribution within the impinging jet

This section presents velocity vector and contour plots of the impinging jet for each measurement plane, along with the corresponding discussions. Since jet velocity distributions can be interpreted by momentum diffusion caused by velocity gradients and the subsequent velocity decay [61], the velocity distributions are examined from the perspective of diffusion based on jet theory.

Fig. 13 illustrates the velocity vector plots obtained from the ultrasonic velocimetry. In the center plane, Case 1 and Case 2 exhibited similar vertical profiles at $r = 0.20$ m. Compared to these cases, Case 3, at $r = 0.20$ m, showed the relatively lower near-floor velocity, while the

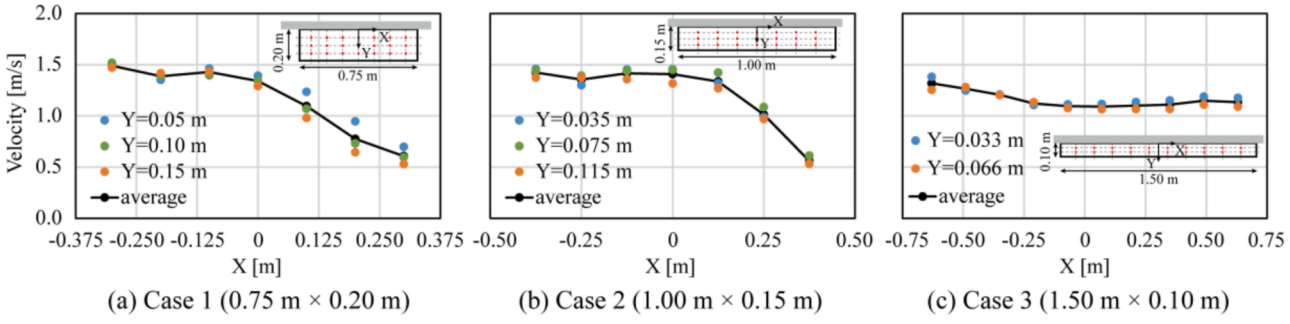

Fig. 11. Velocity distribution in inlet plane.

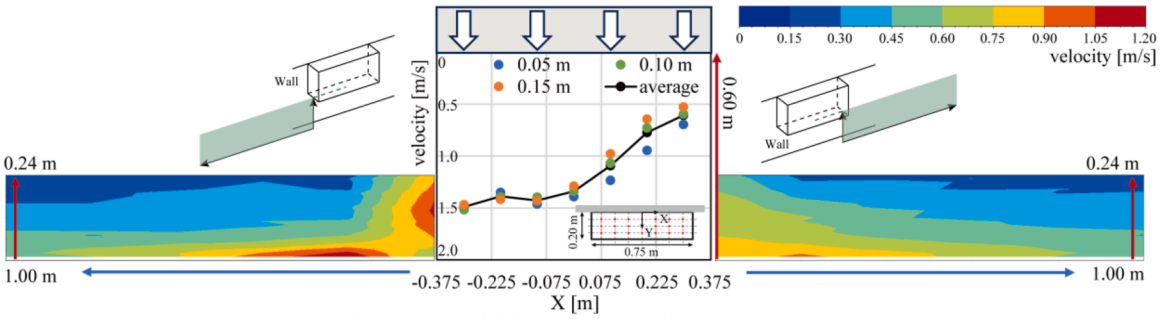

(a) Comparison of side plane: Case 1 (0.75 m × 0.20 m)

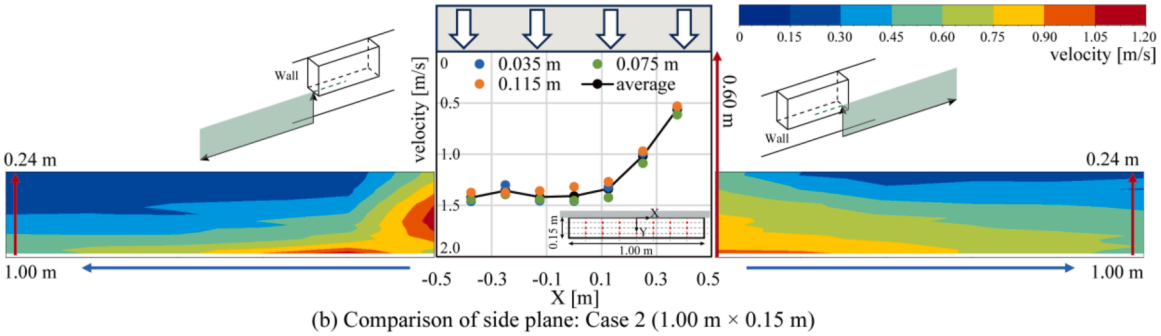

(b) Comparison of side plane: Case 2 (1.00 m × 0.15 m)

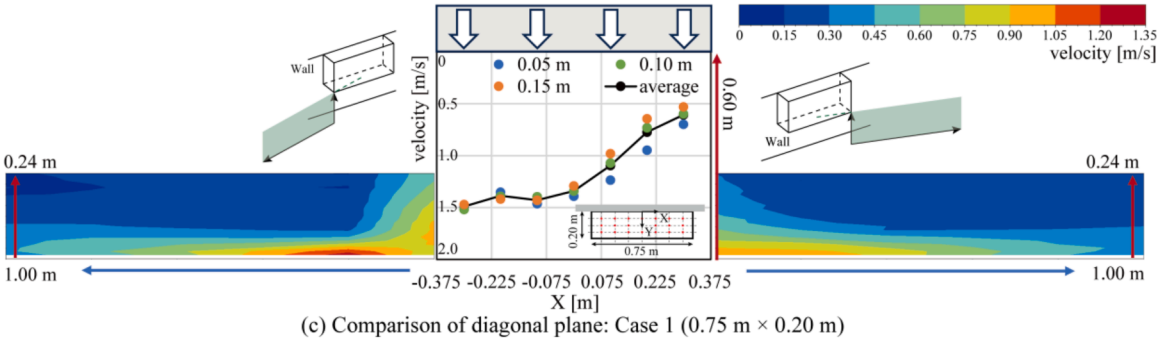

(c) Comparison of diagonal plane: Case 1 (0.75 m × 0.20 m)

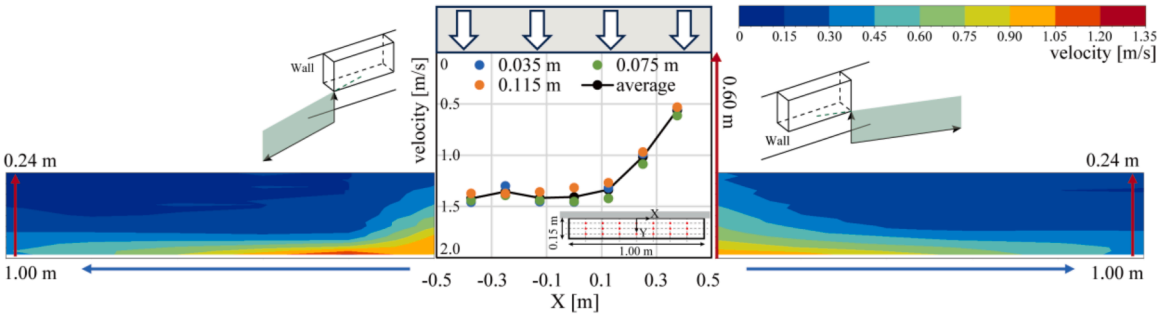

(d) Comparison of diagonal plane: Case 2 (1.00 m × 0.15 m)

Fig. 12. Comparison between right and left plane.

jet maintains higher velocities in the upper regions away from the floor. This finding is consistent with a previous study [44], which reported that a higher aspect ratio results in a larger jet width (i.e., enhanced vertical momentum expansion of the airflow) in the region close to the supply duct.

However, as the jet developed to $r = 1.00$ m, Case 3 presented the highest velocity, followed by Case 2 and Case 1 in descending order. In other words, higher aspect produced higher velocity distribution with jet development at $r = 1.00$ m. This phenomenon can be attributed to the flow characteristics associated with the aspect ratio. As the aspect ratio increases, impinging jets tend to exhibit behavior similar to plane turbulent wall jets, which are known to have a lower velocity decay rate compared to radial wall jets [61]. Consequently, Case 3 (high aspect ratio) maintains high momentum in the primary flow direction (Y-direction). Conversely, Case 1 and Case 2 exhibit behavior closer to a radial jet, promoting horizontal dispersion and resulting in a more rapid velocity decay.

Fig. 13 (b), the right-side plane, shows that the velocity magnitude at $r = 0.20$ m followed the order of Case 2 > Case 1 > Case 3, and this tendency was consistently maintained up to $r = 1.00$ m. The distinctly

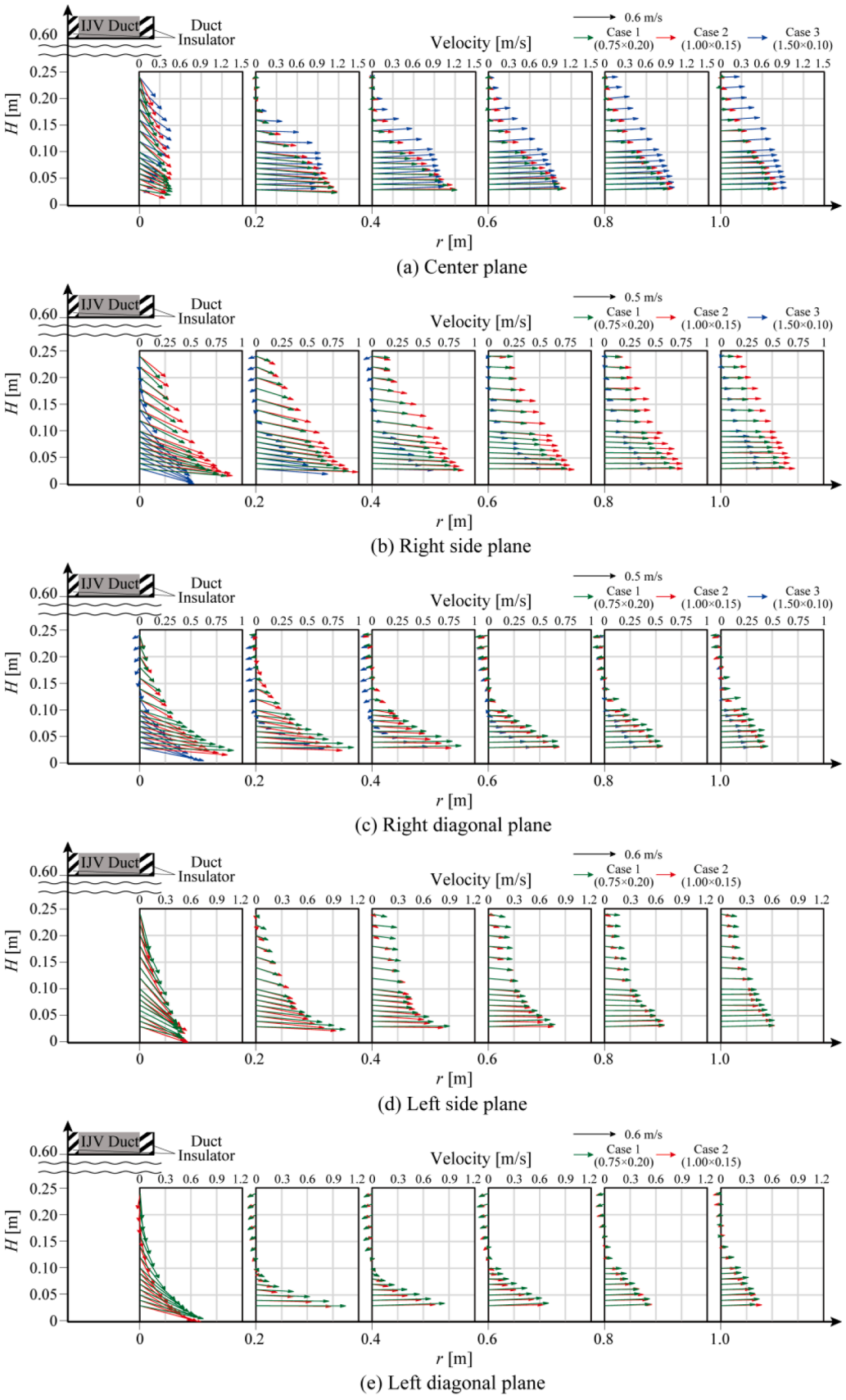

Fig. 13. Velocity vector plot.

lower velocity of Case 3 in the side plane confirms that its flowrate is concentrated in the Y-direction (toward the heat source) due to its planar jet characteristics, reducing the air supply in the X-direction. In the left-side plane, Case 1 and Case 2 showed similar velocity distribution in the overall region.

For the diagonal planes, as presented in Fig. 13 (c) and (e), Case 1 exhibits the highest velocity in the region of $r < 0.4$ m, while its profile subsequently converges to a level similar to that of Case 2. This trend indicates that Case 1 experiences the most rapid velocity decay, attributed to its flow characteristics resembling a radial jet.

Fig. 14 presents the velocity contour plots derived from omnidirectional anemometers. Consistent with the vector analysis, in the center plane, Case 3 reveals that high velocities are sustained in regions above $H > 0.12$ m. Case 3 exhibits characteristics of a plane turbulent wall jet, resulting in lower velocity decay near the floor. This sustained momentum enhances vertical diffusion, causing high velocities to persist even in the region of $H > 0.12$ m.

In the right-side plane (Fig. 14, second row), Case 3 exhibits lower velocity distribution compared to the other cases. This is likely because the airflow in Case 3 is predominantly directed in the Y-direction (towards the heat source), resulting in a relatively smaller airflow rate being supplied to the side directions.

In the diagonal planes, enhanced velocity decay was observed compared to the center and side planes. This is likely due to minimal airflow rate to these directions and interference from the center and side jets [56]. Furthermore, Case 3 exhibited the greatest difference in velocity distribution among each direction. This also confirms that Case 3 has the characteristics of planar jet, whereas the other cases are close to radial jet.

3.3.3. *Influence of supply terminal shape on the stratification height*

It is well known that the indoor environment in stratified ventilation is determined by the balance between the buoyancy-driven flow of thermal plumes and the momentum-dominated flow from the supply airflow. Since the supply terminal geometry was the sole variable in this study under the same airflow rate conditions, it directly alters the impinging jet. As the thermal plume is shaped by the interaction between this jet and the heat source, the indoor environment is dominantly governed by the impinging jet's characteristics. Furthermore, Fig. 13 indicates that velocities at the upper measurement limit ($H = 0.24$ m, $r \geq 0.2$ m) are already very low (< 0.3 m/s). Therefore, we conclude that the flow variations within the measured near-floor region represent the root cause driving the changes in the indoor environment.

The stratification height is theoretically determined by the equilibrium level where the supply airflow rate balances with the thermal plume flow rate. However, the results in Section 3.2.2 demonstrate that the stratification height varies depending on the supply terminal shape under high airflow conditions. This implies that the variation in the supply terminal shape alters the thermal plume flow rate.

This phenomenon can be explained by the airflow characteristics near the heat source. As mentioned above, Case 3 exhibits a notably higher velocity distribution at a radial distance of $r = 1.0$ m. This suggests that the airflow rate directed towards the heat source is greatest compared to the other cases. Previous studies [62,63] reported that supply flow conditions affect turbulence and velocity near the heat source. These local flow characteristics could enhance ambient air entrainment, resulting in a higher plume flowrate. Similarly, we attribute the increased plume flow rate in Case 3 to enhanced entrainment driven by the higher velocity field surrounding the heat source. Furthermore, when the high-momentum jet in Case 3 impinges on the heating element, it generates high-velocity airflow and significant

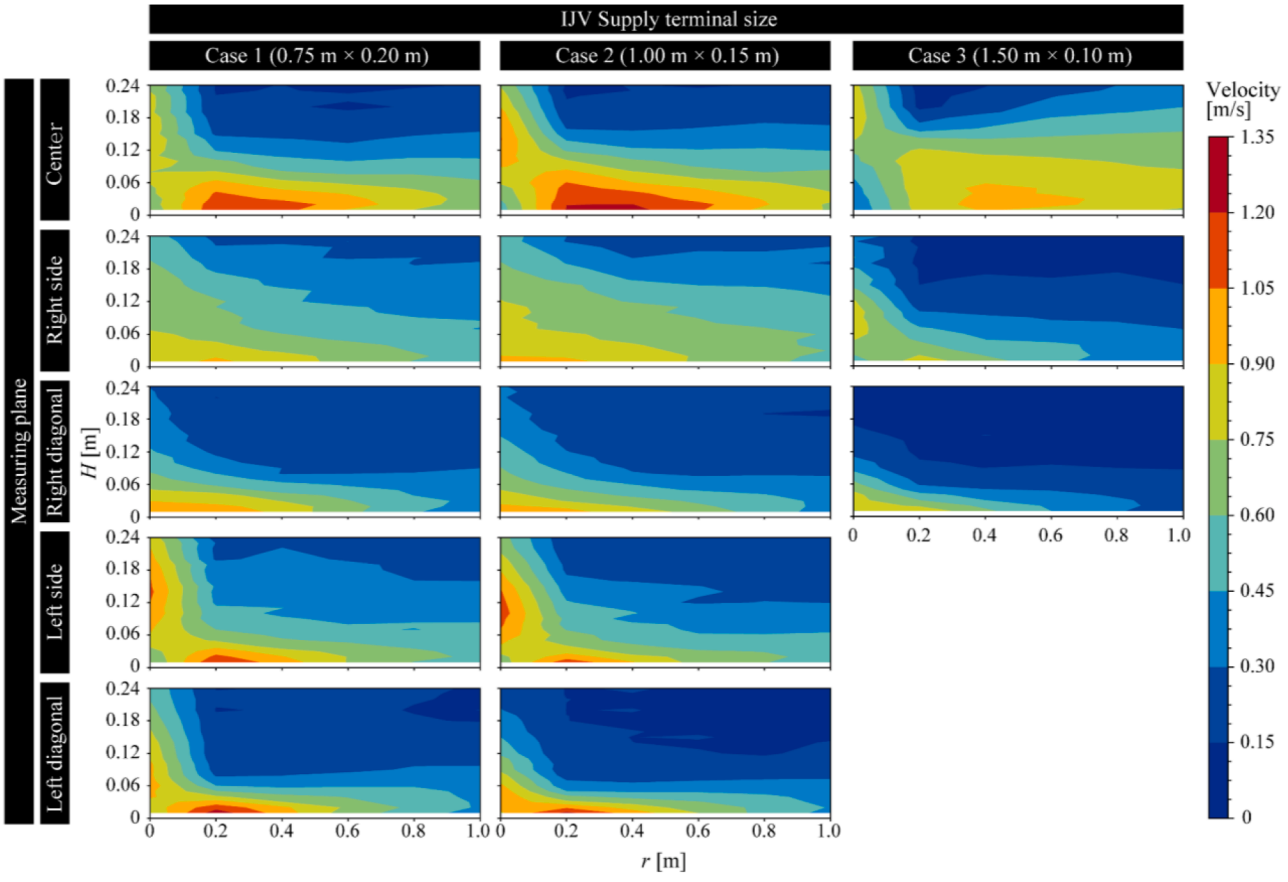

Fig. 14. Velocity contour plot.

turbulence as the flow moves along the heating element. In addition to the enhanced entrainment, this could cause a direct increase in the upward airflow rate after impingement.

However, direct measurements of the plume velocity distribution were not conducted in this study. To fully elucidate this phenomenon, further investigations using CFD or comprehensive airflow experiments are required.

4. Conclusions

In this study, full-scale experiments were conducted to examine the influence of IJV supply terminal shape on the indoor environment and airflow characteristics. The supply terminal shape was configured in three different shapes with the same areas but varying the aspect ratios. The temperature and CO_2 concentration were measured to investigate the indoor environment, and velocity data were obtained to analyze the cause of variations in the indoor environment resulting from the supply terminal shape differences.

Dimensionless temperature, dimensionless CO_2 concentration, stratification height, HRE, and CRE were analyzed to evaluate the indoor environment, and the velocity data for impinging jets were investigated to examine the mechanism by which the supply terminal shape affects the indoor temperature and CO_2 concentration.

The main findings from the experimental results are outlined as follows:

- •The dependence of the indoor environment (e.g., temperature and CO_2 concentration) on the supply terminal shape varied with the supply airflow rate. This variation appeared to be governed by the Archimedes number (Ar_{room}), which represents the ratio of buoyancy to momentum forces. The threshold value was approximately 1.2 in the present study.
- •Buoyancy-dominated regime ($Ar_{room} > 1.2$): Under conditions of low supply airflow momentum, the supply terminal shape has a negligible impact on the indoor environment.
- •Momentum-dominated regime ($Ar_{room} < 1.2$): As the supply momentum increases, the indoor environment becomes highly sensitive to the terminal shape.

- Impact of aspect ratio: the dimensionless temperature and CO_2 concentration distributions tended to rise with an increase in the aspect ratio of the supply terminal. In addition, the stratification height presented a decreasing tendency as the aspect ratios increased, implying higher plume flow rates. As a result, HRE and CRE showed decrease tendency as the aspect ratio become higher.
- Velocity distribution: The velocity distribution results suggest that the impinging jets may show the characteristics for either two-dimensional or radial jet contingent upon the shape of the supply terminal. As a result, it is expected that the airflow distribution patterns or the velocity of airflow reaching the heating element are changed, leading to the variation in the flow rate of the thermal plume.

In this study, the velocity distribution was measured in limited areas and the plume flow rate was not investigated quantitatively. Also, the proposed Ar_{room} threshold was derived based on specific conditions using slit-type supply terminals. Therefore, further studies are required to investigate detailed plume characteristics and to verify applicability of the Ar_{room} threshold to other parameters such as different inlet shapes (e.g., circular or semi-elliptical), varying heat densities, and different room dimensions. Despite these limitations, this study underlines the importance of supply terminal shape and illustrates its impact on the indoor environment under the IJV system.

As a future prospect, in order to clearly elucidate the principle by which the supply terminal shape affects the indoor environment, further studies are need to investigate the comprehensive measurements of indoor airflows.

CRediT authorship contribution statement

Sungeun Lee: Writing – original draft, Validation, Methodology, Investigation, Formal analysis, Data curation, Conceptualization. **Tomohiro Kobayashi:** Writing – review & editing, Supervision, Project administration, Methodology, Funding acquisition, Conceptualization. **Haruna Yamasawa:** Writing – review & editing, Supervision, Methodology, Investigation, Conceptualization. **Kentaro Kida:** Writing – review & editing, Validation, Methodology, Investigation, Data curation.

Declaration of competing interest

This manuscript has not been published or presented elsewhere in part or in entirety and is not under consideration by another journal. We have read and understood your journal's policies, and we believe that neither the manuscript nor the study violates any of these. There are no conflicts of interest to declare.

Acknowledgements

A part of this work was supported by joint research with Osaka Gas Co. Ltd., which is gratefully acknowledged.

Supplementary materials

Supplementary material associated with this article can be found, in the online version, at doi:10.1016/j.buildenv.2026.114329.

Data availability

Data will be made available on request.

References

[1] European Commission, The European green deal, Eur. Community (2019) 1–24. https://eur-lex.europa.eu/legal-content/EN/TXT/PDF/?uri=CELEX:52019DC0640&from=EN (accessed May 23, 2025).
[2] UK Government, UKCOP26.ORG:COP26 Goals - UN Clim. Change Conf. (COP26) SEC – Glasg. 2021 (2021). https://ukcop26.org/cop26-goals/ (accessed May 23, 2025).
[3] Ministry of Climate and Enterprise of Sweden, Swedish climate solutions. https://government.se/articles/2025/05/the-swedish-offer-to-support-ambitious-climate-plans/, 2025.
[4] Ministry of Environment of Japan, Climate actions towards net-zero by 2050. http://www.env.go.jp/earth/26cop2616cmp16cma10311112.html, 2021.
[5] A. Melikov, A. Li, R. Kosonen, X. Li, Occupant targeted ventilation brings clean air to occupants, REHVA Eur. HVAC J. 49 (2022). https://www.researchgate.net/publication/358915595.
[6] X. Yuan, Q. Chen, L.R. Glicksman, A critical review of displacement ventilation, ASHRAe Trans. 104 (1A) (1998) 78–90.
[7] O.A. Seppanen, W.J. Fisk, J. Eto, D.T. Grimsrud, Comparison of conventional mixing and displacement air-conditioning and ventilating systems in U.S. commercial buildings, ASHRAe Trans. 95 (2) (1989) 1028–1040.
[8] R. Kosonen, A. Melikov, E. Mundt, P. Mustakallio, P.V. Nielsen, REHVA Guidebook No 23 - displacement ventilation, REHVA (Fed. Eur. Heat. Air-cond. Assoc.) (2017).
[9] M. Sandberg, C. Blomqvist, Displacement ventilation systems in office rooms, ASHRAe Trans. 95 (2) (1989) 1041–1049.
[10] H.M. Mathisen, Case studies of displacement ventilation in public halls, ASHRAe Trans. 95 (2) (1989) 1018–1027.
[11] P.V Nielsen, Temperature distribution in a displacement ventilation room, in:, in: 5th International Conference on Air Distribution in Rooms, ROOMVENT, 1996, pp. 323–329.
[12] X. Yuan, Q. Chen, L.R. Glicksman, Y. Hu, X. Yang, Measurements and computations of room airflow with displacement ventilation, ASHRAe Trans. 105 (1) (1999) 340–352.
[13] T. Suzuki, K. Sagara, T. Yamanaka, H. Kotani, T. Yamashita, Vertical profile of contaminant concentration in sickroom with lying person ventilated by displacement, in: in:, in: proceedings of IAQVEC 2007 - the 6th International Conference on Indoor Air Quality, Ventilation & Energy Conservation in Buildings, 2007.
[14] Y. Li, M. Sandberg, L. Fuchs, Vertical temperature profiles in rooms ventilated by displacement: full-scale measurement and nodal modelling, Indoor. Air. 2 (1992) 225–243, https://doi.org/10.1111/J.1600-0668.1992.00005.X.

[15] M. Xu, T. Yamanaka, H. Kotani, Vertical profiles of temperature and contaminant concentration in rooms ventilated by displacement with heat loss through room envelopes, Indoor. Air. 11 (2001) 111–119, https://doi.org/10.1034/J.1600-0668.2001.110205.X.
[16] N. Choi, T. Yamanaka, K. Sagara, Y. Momoi, T. Suzuki, Displacement ventilation with radiant panel for hospital wards: measurement and prediction of the temperature and contaminant concentration profiles, Build Env. (2019) 160, https://doi.org/10.1016/j.buildenv.2019.106197.
[17] P.V Nielsen, Displacement Ventilation - Theory and Design, Aalborg University, Denmark, 1993.
[18] T. Yamanaka, H. Kotani, M. Xu, Zonal models to predict vertical contaminant distribution in room with displacement ventilation accounting for convection flows along walls, in:, in: 10th International Conference on Air Distribution in Rooms, ROOMVENT 20070, 2007.
[19] N.M. Mateus, G. Carrilho da Graça, A validated three-node model for displacement ventilation, Build Env. 84 (2015) 50–59, https://doi.org/10.1016/j.buildenv.2014.10.029.
[20] N. Choi, T. Yamanaka, T. Kobayashi, T. Ihama, M. Wakasa, Influence of vertical airflow along walls on temperature and contaminant concentration distributions in a displacement-ventilated four-bed hospital ward, Build Env. 183 (2020) 107181, https://doi.org/10.1016/J.BUILDENV.2020.107181.
[21] H. Xing, H.B. Awbi, Measurement and calculation of the neutral height in a room with displacement ventilation, Build Env. 37 (2002) 961–967, https://doi.org/10.1016/S0360-1323(01)00079-8.
[22] S. H, S. M, M. M, Dispersion pattern of contaminants in a displacement ventilated room - implications for demand control, in:, in: air Movement & Ventilation Control within Buildings, 12th AIVC Conference, 1991, pp. 173–189. https://www.aivc.org/resource/dispersion-pattern-contaminants-displacement-ventilated-room-implications-demand-control (accessed May 23, 2025).
[23] X. Yuan, Q. Chen, M.R. ASHRAE Leon Glicksman, Models for prediction of temperature difference and ventilation effectiveness with displacement ventilation, ASHRAe Trans. 105 (1999) 353–367, 1.
[24] A. Melikov, J. Nielsen, Local thermal discomfort due to draft and vertical temperature difference in rooms with displacement ventilation, ASHRAe Trans. (1989) 1050–1057.
[25] T. Karimipanah, Turbulent Jets in Confined Spaces, University of Gavle, 1996.
[26] T. Karimipanah, H.B. Awbi, Theoretical and experimental investigation of impinging jet ventilation and comparison with wall displacement ventilation, Build Env. 37 (2002) 1329–1342, https://doi.org/10.1016/S0360-1323(01)00117-2.
[27] H. Awbi, Ventilation of Buildings, 2nd edition, Routledge, 2002.
[28] T. Karimipanah, M. Sandberg, H.B. Awbi, A comparative study of different air distribution systems in a classroom, in: in: roomvent Read. (2000) 1013–1018.
[29] G. Cao, H. Awbi, R. Yao, Y. Fan, K. Sirén, R. Kosonen, J. (Jensen) Zhang, A review of the performance of different ventilation and airflow distribution systems in buildings, Build Env. 73 (2014) 171–186, https://doi.org/10.1016/j.buildenv.2013.12.009.
[30] ASHRAE, ASHRAE Standard 55-2020: thermal environmental conditions for Human occupancy, 2021.
[31] ISO, ISO-7730, ergonomics of the Thermal environment - analytical determination and interpretation of thermal comfort using calculation of the PMV and PPD indices and local thermal comfort criteria, 2005.
[32] B. Yang, A.K. Melikov, A. Kabanshi, C. Zhang, F.S. Bauman, G. Cao, H. Awbi, H. Wigö, J. Niu, K.W.D. Cheong, K.W. Tham, M. Sandberg, P.V. Nielsen, R. Kosonen, R. Yao, S. Kato, S.C. Sekhar, S. Schiavon, T. Karimipanah, X. Li, Z. Lin, A review of advanced air distribution methods - theory, practice, limitations and solutions, Energy Build. (2019) 202, https://doi.org/10.1016/j.enbuild.2019.109359.
[33] A. Ameen, M. Cehlin, U. Larsson, T. Karimipanah, Experimental investigation of the ventilation performance of different air distribution systems in an office environment—Cooling mode, Energies (2019) 1354, https://doi.org/10.3390/EN12071354, 2019, Vol. 12, Page 1354 12.
[34] A. Ameen, M. Cehlin, H. Yamasawa, T. Kobayashi, T. Karimipanah, Energy saving, indoor thermal comfort and indoor air quality evaluation of an office environment using corner impinging jet ventilation, Dev. Built Environ. 15 (2023), https://doi.org/10.1016/j.dibe.2023.100179.
[35] M. Fan, Z. Fu, J. Wang, Z. Wang, H. Suo, X. Kong, H. Li, A review of different ventilation modes on thermal comfort, air quality and virus spread control, Build Env. 212 (2022), https://doi.org/10.1016/j.buildenv.2022.108831.
[36] L. Wang, X. Dai, J. Wei, Z. Ai, Y. Fan, L. Tang, T. Jin, J. Ge, Numerical comparison of the efficiency of mixing ventilation and impinging jet ventilation for exhaled particle removal in a model intensive care unit, Build Env. 200 (2021), https://doi.org/10.1016/j.buildenv.2021.107955.
[37] X. Ye, H. Zhu, Y. Kang, K. Zhong, Heating energy consumption of impinging jet ventilation and mixing ventilation in large-height spaces: a comparison study, Energy Build. 130 (2016) 697–708, https://doi.org/10.1016/j.enbuild.2016.08.055.
[38] X. Ye, Y. Kang, X. Yang, K. Zhong, Temperature distribution and energy consumption in impinging jet and mixing ventilation heating rooms with intermittent cold outside air invasion, Energy Build. 158 (2018) 1510–1522, https://doi.org/10.1016/j.enbuild.2017.11.038.
[39] H. Yamasawa, T. Kobayashi, T. Yamanaka, N. Choi, M. Cehlin, A. Ameen, Applicability of displacement ventilation and impinging jet ventilation system to heating operation, Jpn. Archit. Rev. 4 (2021) 403–416, https://doi.org/10.1002/2475-8876.12220.
[40] T. Kobayashi, N. Umemiya, Simplified prediction using block model for vertical profile of temperature and contaminant concentration in a room with impinging jet ventilation, Build Env. 209 (2022) 108643, https://doi.org/10.1016/j.buildenv.2021.108643.
[41] J. Hu, Y. Kang, Y. Lu, J. Yu, K. Zhong, Simplified models for predicting thermal stratification in impinging jet ventilation rooms using multiple regression analysis, Build Env. (2021) 206, https://doi.org/10.1016/j.buildenv.2021.108311.
[42] H. Yamasawa, T. Kobayashi, T. Yamanaka, N. Choi, M. Cehlin, A. Ameen, Effect of supply velocity and heat generation density on cooling and ventilation effectiveness in room with impinging jet ventilation system, Build Env. 205 (2021) 108299, https://doi.org/10.1016/j.buildenv.2021.108299.
[43] H.J. Chen, B. Moshfegh, M. Cehlin, Investigation on the flow and thermal behavior of impinging jet ventilation systems in an office with different heat loads, Build Env. 59 (2013) 127–144, https://doi.org/10.1016/J.BUILDENV.2012.08.014.
[44] H.J. Chen, B. Moshfegh, M. Cehlin, Numerical investigation of the flow behavior of an isothermal impinging jet in a room, Build Env. 49 (2012) 154–166, https://doi.org/10.1016/j.buildenv.2011.09.027.
[45] A. Staveckis, A. Borodinecs, Impact of impinging jet ventilation on thermal comfort and indoor air quality in office buildings, Energy Build. 235 (2021) 110738, https://doi.org/10.1016/j.enbuild.2021.110738.
[46] C. Wang, X. Zhang, K. Hu, Y. Liu, Geometric-parameter influence and orthogonal evaluation on the thermal environment for an impinging jet ventilation system inlet, Case Stud. Therm. Eng. 51 (2023), https://doi.org/10.1016/j.csite.2023.103573.
[47] H. Chen, B. Moshfegh, M. Cehlin, Computational investigation on the factors influencing thermal comfort for impinging jet ventilation, Build Env. 66 (2013) 29–41, https://doi.org/10.1016/j.buildenv.2013.04.018.
[48] X. Yang, X. Ye, B. Zuo, K. Zhong, Y. Kang, Analysis of the factors influencing the airflow behavior in an impinging jet ventilation room, Build. Simul. 14 (2021) 749–762, https://doi.org/10.1007/S12273-020-0690-6/METRICS.
[49] X. Ye, H. Qi, Y. Kang, K. Zhong, Optimization study of heating performance for an impinging jet ventilation system based on data-driven model coupled with TOPSIS method, Build Env. 223 (2022), https://doi.org/10.1016/j.buildenv.2022.109465.
[50] T. Kobayashi, K. Sugita, N. Umemiya, T. Kishimoto, M. Sandberg, Numerical investigation and accuracy verification of indoor environment for an impinging jet ventilated room using computational fluid dynamics, Build Env. 115 (2017) 251–268, https://doi.org/10.1016/j.buildenv.2017.01.022.
[51] A. Essa, T. Yamanaka, T. Kobayashi, N. Choi, Effect of source location on contaminant dispersion pattern and occupants inhaled air quality in lecture room under displacement ventilation, Jpn. Archit. Rev. 6 (2023), https://doi.org/10.1002/2475-8876.12313.
[52] O. Han, A. Li, Velocity distribution of wall-attached jets in slotted-inlet ventilated rooms, Build Env. 194 (2021), https://doi.org/10.1016/j.buildenv.2021.107708.
[53] D. Irwin, C. Simonson, K. Saw, R. Besant, Contaminant and heat removal effectiveness and air-to-air heat/energy recovery for a contaminated air space, ASHRAe Trans. 104 (2) (1998) 1–15. https://cris.vtt.fi/en/publications/contaminant-and-heat-removal-effectiveness-and-air-to-air-heatene (accessed May 29, 2025).
[54] SHASE, SHASE Standard 102-2011, Vent. Requir. Accept. Indoor Air Qual. (2011).
[55] E. Mundt, H.M. Mathisen, P.V. Nielsen, A. Moser, REHVA guidebook No 2 - ventilation effectiveness, REHVA (2004).
[56] A. Li, Attachment Ventilation Theory, Springer, Singapore, 2023, https://doi.org/10.1007/978-981-19-9259-9/COVER.
[57] P.V. Nielsen, in: The "Family Tree" of Air Distribution Systems, in: In: 12th INternational Conference on Air Distribution in Rooms (Roomvent, 2011. Digital Media, 2011.
[58] A. Ameen, M. Cehlin, U. Larsson, T. Karimipanah, Experimental investigation of ventilation performance of different air distribution systems in an office environment—Heating mode, Energies 12 (2019) 1835, https://doi.org/10.3390/EN12101835, 2019, Vol. 12, Page 1835.
[59] H. Yamasawa, T. Kobayashi, T. Yamanaka, N. Choi, M. Matsuzaki, Experimental investigation of difference in indoor environment using impinging jet ventilation and displacement ventilation systems, Int. J. Vent. 21 (2022) 229–246, https://doi.org/10.1080/14733315.2020.1864572.
[60] H.J. Park, D. Holland, The effect of location of a convective heat source on displacement ventilation: CFD study, Build Env. 36 (2001) 883–889, https://doi.org/10.1016/S0360-1323(01)00014-2.
[61] N. Rajaratnam, Turbulent Jets, Elsevier Science Ltd., 1976.
[62] Z. Popiolek, Z. Trzeciakiewicz, S. Mietzwmski, Improvement of a plume volume flux calculation model, Proc. ROOMVENT '98 1 (1998) 423–430.
[63] P. Kofoed, P.V Nielsen, in: Thermal plumes in ventilated rooms - Measurements in stratified surroundings and analysis by use of an extrapolation method, RoomVent-90, International Conference, Oslo, Norway, 1990.